APPENDIX B

Publication P4

Repo A.-K., Arkkio A. Numerical impulse response test to identify parametric models for closed-slot deep-bar induction motors. *IET Electric Power Applications*, Vol. 1, No. 3, May 2007, pp. 307-315.

Numerical impulse response test to identify parametric models for closed-slot deep-bar induction motors

A.-K. Repo and A. Arkkio

Abstract: An impulse response test for estimating the electrical parameters of a deep-bar induction motor is studied. The impulse response test is performed within the two-dimensional finite-element analysis (FEA). The impulse excitation is applied to the stator voltage. Since the test is suitable for modelling the perturbations about a certain operation point, a small-signal model for the double-cage induction machine is derived. The skin effect is taken into account by using two parallel rotor branches. In addition to the small-signal parameters, the steady-state parameters are also estimated using the time-harmonic FEA. The impulse response test is based on the assumption of linear behaviour about an operation point. Thus, the effects of nonlinearity are studied by several methods.

1 Introduction

The finite-element analysis (FEA) is an accurate and widely applied method in the study and simulation of electrical machines. With the numerical magnetic field analysis, features which can be difficult, expensive or even impossible to measure can be explored. On the other hand, a simpler equivalent circuit model for the machine is required in many applications. The performance and applicability of the circuit model depend on both the structure of the model and the accuracy of the parameters. Besides an accurate simulation method, the FEA can be seen as a tool for obtaining the circuit parameters. In many previous works [1–3], the time-harmonic field solution has been used to derive the steady-state equivalent circuit parameters.

This paper continues from the observations made in [4]. In [4], the parameters of a small-signal model derived from the basic T-equivalent circuit were estimated using the frequency response function (FRF) of the stator current. The FRF was obtained from the numerical impulse response test performed within the two-dimensional time-stepping analysis. It was concluded that the rotor parameters are strongly frequency-dependent, which has to be taken into account in the model when fitting the frequency response data. The aim of this paper is to include the skin effect in the small-signal model adding another rotor branch to the equivalent circuit. The small-signal parameters are related to the incremental or transient permeability and they are required for designing and adjusting control algorithms. The saturation is also studied in more detail, and the impulse test is refined in order to obtain better results. The influence of saturation on small-signal model parameters has been studied in [5].

doi:10.1049/iet-epa:20060436

Paper first received 1st November 2006 and in revised form 16th January 2007

The authors are with the Laboratory of Electromechanics, Helsinki University of Technology, P.O.Box 3000, TKK FI-02015, Finland

E-mail: anna-kaisa.repo@tkk.fi

More advanced state-space models including the skin effect have been presented, for example, in [6, 7]. In these models, one or more additional rotor branches were included to the basic equivalent circuit, and the rotor currents of the new branches act as additional state variables. In [8], the skin effect was also taken into account by using an additional parallel branch. The rotor parameters were measured from the locked rotor tests. The responses of an induction machine to the small perturbations in the stator voltage, supply frequency and load torque were defined by measurements. These were compared with several analytical models. It was shown that even at frequencies <80 Hz the skin effect had an importance in the case of the studied double-cage rotor. A more advanced rotor model was proposed in [9]. The steady-state equivalent circuit was modified by replacing the linear part of the rotor impedance with a transfer function the order and coefficients of which were estimated from a measured frequency response at standstill. The rotor model was therefore a small-signal model without any definite interpretation of the physical parameters.

The steady-state parameters of a double-cage model are also estimated. The method applied is referred as the impedance method. In this case, the time-harmonic FEA and the effective permeability [10] are applied. The obtained parameters are able to depict the rms-valued voltages and currents. In order to distinguish the two cases, the steady-state parameters are denoted with capital and small-signal parameters with lower-case letters.

2 Methods

2.1 Circuit model

Fig. 1 presents a double-cage rotor model with nine physical parameters. The rotor resistances are divided by the slip.

The two parallel rotor branches consist of the resistance and leakage reactance. The rotor bars have common end-rings and their effect is modelled by resistance R_c

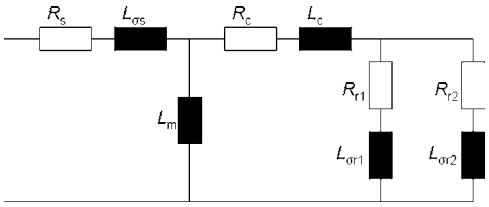

Fig. 1 *Equivalent circuit for the double-cage induction machine*

and inductance L_c. In the approach of [6], the rotor branches are assumed to be equal in the way that both of the rotor currents flow through the mutual components L_c and R_c. This can be interpreted as if the cross-section of the rotor slot was divided into two sub-conductors. Using the same approach as in [6], the voltage and flux linkage equations in the reference frame rotating at speed ω_k can be written as

$$\underline{u}_s^k = R_s \underline{i}_s^k + \frac{d\underline{\psi}_s^k}{dt} + j\omega_k \underline{\psi}_s^k \quad (1)$$

$$\underline{u}_{r1}^k = (R_{r1} + R_c)\underline{i}_{r1}^k + R_c \underline{i}_{r2}^k + \frac{d\underline{\psi}_{r1}^k}{dt} + j(\omega_k - \omega_r)\underline{\psi}_{r1}^k \quad (2)$$

$$u_{r2}^k = R_c \underline{i}_{r1}^k + (R_c + R_{r2})\underline{i}_{r2}^k + \frac{d\underline{\psi}_{r2}^k}{dt} + j(\omega_k - \omega_r)\underline{\psi}_{r2}^k \quad (3)$$

$$\underline{\psi}_s^k = (L_m + L_{\sigma s})\underline{i}_s^k + L_m(\underline{i}_{r1}^k + \underline{i}_{r2}^k) \quad (4)$$

$$\underline{\psi}_{r1}^k = L_m \underline{i}_s^k + (L_m + L_c + L_{\sigma r1})\underline{i}_{r1}^k + (L_m + L_c)\underline{i}_{r2}^k \quad (5)$$

$$\underline{\psi}_{r2}^k = L_m \underline{i}_s^k + (L_m + L_c)\underline{i}_{r1}^k + (L_m + L_c + L_{\sigma r2})\underline{i}_{r2}^k \quad (6)$$

where superscript k refers to the reference frame. Equation of motion is defined as

$$T_L = -\frac{J}{p}\frac{d\omega_r}{dt} + \frac{3}{2}pL_m \, \mathrm{Im}\{\underline{\psi}_s^* \underline{i}_s\} \quad (7)$$

p is the number of pole pairs and J the mass of inertia of the rotor. The small-signal model can be derived from voltage and flux equations (1)–(6) by assuming small disturbances in the voltages, currents and flux linkages [11]. At this stage, the rotor speed, supply frequency and load torque are kept constant. The small-signal model of the induction machine is simplest to define in the synchronous reference frame in which the steady-state quantities are stationary. Here, the small-signal model is presented in Laplace domain. With frequency-dependent short-notations

$$\begin{aligned}
\underline{z}_s(s) &= r_s + sl_{\sigma s} + j\omega_k l_{\sigma s} \\
\underline{z}_m(s) &= sl_m - j\omega_0 l_m + j\omega_k l_m \\
\underline{z}'_m(s) &= sl_m + j\omega_k l_m \\
z_c(s) &= r_c + sl_c - j\omega_0 l_c + j\omega_k l_c \\
\underline{z}_1(s) &= r_{r1} + sl_{\sigma r1} - j\omega_0 l_{\sigma r1} + j\omega_k l_{\sigma r1} \\
\underline{z}_2(s) &= r_{r2} + sl_{\sigma r2} - j\omega_0 l_{\sigma r2} + j\omega_k l_{\sigma r2}
\end{aligned} \quad (8)$$

the small-signal model can be presented in the form

$$\frac{\Delta \underline{i}_s^k}{\Delta \underline{u}_s^k} = \frac{(\underline{z}_1 + \underline{z}_2)(\underline{z}_m + \underline{z}_c) + \underline{z}_1 \underline{z}_2}{(\underline{z}_1 + \underline{z}_2)(\underline{z}_s \underline{z}_m + \underline{z}_s \underline{z}_c + \underline{z}'_m \underline{z}_c) + \underline{z}_1 \underline{z}_2 (\underline{z}_s + \underline{z}'_m)} \quad (9)$$

The number of the physical parameters in the double-cage circuit model can be less than that shown in Fig. 1. Either one or both of the mutual rotor parameters X_c and R_c can be neglected and their effect can be included in the remaining rotor parameters [12, 13]. The subject is discussed in detail in Section 3.2.

2.2 Impedance method

The steady-state parameters of the equivalent circuit can be derived using the concept of impedance matrix [2]. From the couplings between the stator and rotor conductors, a large coupling matrix can be constructed. This matrix can be suppressed to correspond to the circuit model using the symmetric components. To obtain multiple-cage circuit models, the rotor bars can be divided into several sub-conductors. The details of the method are given in [14].

2.3 Impulse response test

The aim of the impulse test is to obtain the FRF corresponding to the one obtained using the harmonic excitation. The term 'harmonic excitation' refers to a method in which a single excitation frequency component is added, for example, to the supply voltage. Therefore it is a very time-consuming method when using the time-stepping analysis. The purpose of the impulse test is to excite several frequencies at the same time and thus reduce the number of simulations required.

For the linear system, the response signal, for example, the stator current, is non-zero only at the excitation frequency. In the case of the nonlinear system, the response signal may contain other frequencies. If the amplitudes of the excess components are very small compared with the excited frequency, they can be neglected. Within the numerical harmonic excitation, only the frequency response at the excitation frequency is taken into account when calculating the FRF. The features of the harmonic excitation are discussed in detail in Section 4. Since the linear model (9) cannot include the influence of the excess harmonics, they have to be cancelled or minimised in the case of impulse test as well.

Next, two different methods to obtain the FRF with impulse test are presented. The impulse test is performed within a two-dimensional time-stepping FEA, which takes into account the magnetic saturation, skin effect in the rotor bars and rotation of the rotor. The time step of FEA is 50 μs. The impulse excitation is added to the steady-state line-to-line voltage vector $\underline{v}_s$, which rotates at the supply frequency ω_s.

2.3.1 Impulse test with one impulse: In [4], a suitable impulse type was looked for by performing impulse tests with several different impulse types. The chosen impulse type was defined by

$$\underline{v}_s + \Delta \underline{v}_s = |\underline{v}_s| e^{j\omega_s t} + |\Delta \underline{v}_s(t)| \quad (10)$$

$$|\Delta \underline{v}_s(t)| = \begin{cases} a_{rel}\hat{v}\sin^3(4\pi f_d t) + c a_{rel}\hat{v}\sin^2(2\pi f_d t), \\ 0, \end{cases} \quad \begin{array}{l} t_1 \le t \le t_1 + t_d \\ \text{otherwise} \end{array} \quad (11)$$

where the duration time t_d was 5.0 ms, f_d was 100 Hz and relative amplitude a_{rel} was 5%. f_d defines the shape and t_1 starting time of impulse. Since the impulse does not rotate

in the stator frame of reference, it rotates with respect to the voltage vector.

This type of impulse was chosen since its amplitude at zero frequency can be controlled by coefficient c. The amplitude has to be low since, due to small stator resistance, the gain for the current is high at zero frequency. A suitable value $c = 2\%$ was found performing several impulse tests. With these settings, the peak of the current transient is 7% of the rated current. The simulation is run until the transient of the stator current has completely decayed. Usually, 10 000 time steps are adequate and the zero padding can be used to increase the frequency resolution.

An electrical machine produces certain frequencies also at the steady-state operation. For example, the amplitude of the supply frequency component is very high compared with the frequency components of the impulse excitation. In order to cancel the natural frequencies, the impulse test is performed twice with both positive and negative amplitudes. The simulation results are then subtracted from each other. Another option is to simulate the steady state without an impulse and subtract it from the disturbed case. This can be a more useful alternative if several different impulse tests are performed at the same operation point. The difference in the resulting FRF is negligibly small.

Since the small-signal model is derived for the phase variables, $\Delta\underline{u}_s^k$ is computed from the voltages across the stator phase windings and $\Delta\underline{u}_s^k$ from the phase currents. These are transformed to the frequency domain using FFT, and from the ratio, the FRF of the stator current is obtained. Fig. 2 illustrates the impulse detected by the space vector of phase voltages in the synchronous reference frame. Arrows depicting the impulse are presented at every 0.25 ms and magnified by ten.

The impulse defined by (10) can be considered as a continuous distribution of excitation frequencies with varying phase angle with respect to the supply voltage.

2.3.2 Impulse test with two impulses: The impulse can also be synchronised with the supply voltage and only a single value for the phase angle can be determined. The direction of the impulse is now calculated at each time step so that it has an angle φ with respect to the total voltage vector

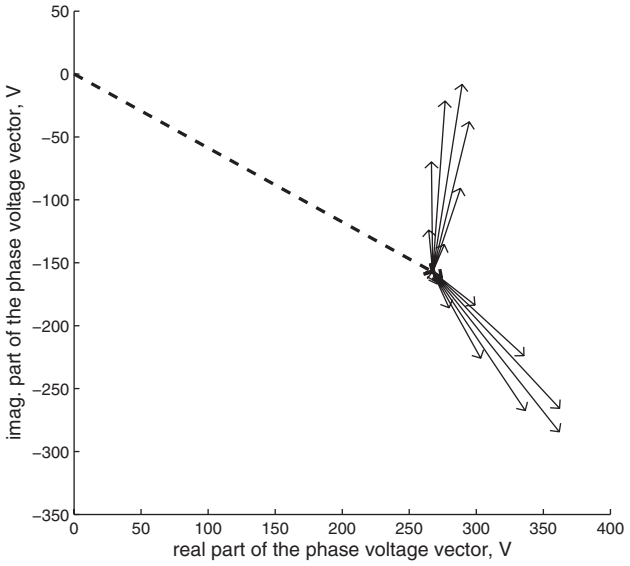

Fig. 2 *Impulse to the phase voltage vector (steady-state with dashed line)*

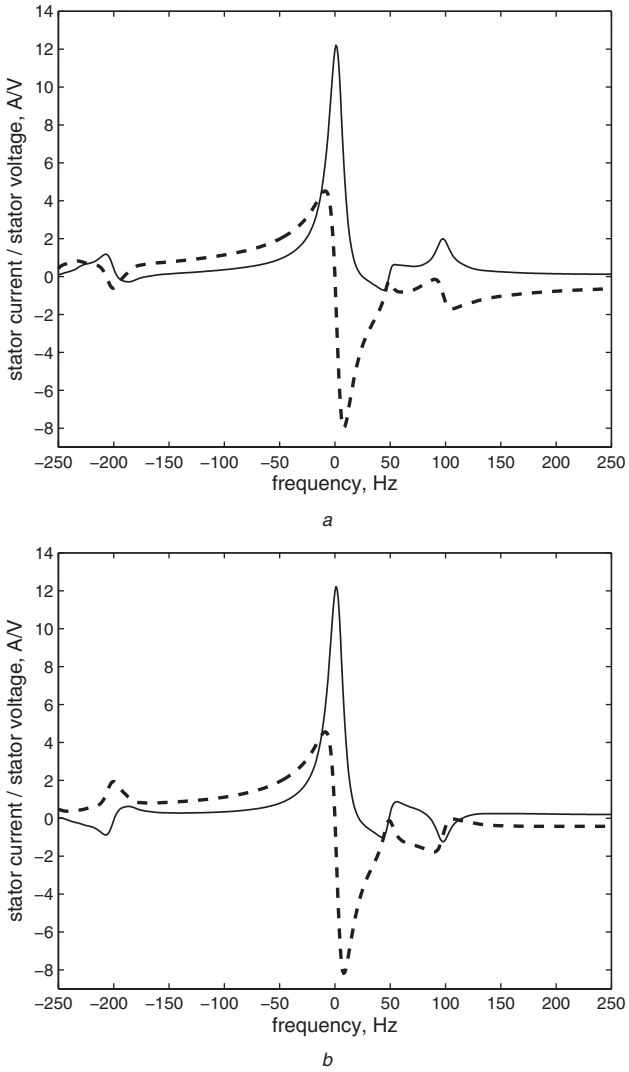

Fig. 3 Average of two FRFs

a FRF obtained with $\varphi = 0$

b FRF obtained with $\varphi = \pi/2$ (Real parts with solid line, imaginary parts with dashed line)

$$\underline{v}_s + \Delta\underline{v}_s = |\underline{v}_s|e^{j\omega_{st}} + |\Delta\underline{v}_{s(t)}|e^{j(\omega_s t+\varphi)} \tag{12}$$

Since only one direction is considered, the time-dependence of the amplitude of the voltage impulse is defined by

$$|\Delta\underline{v}_s(t)| = \begin{cases} a_{rel}\hat{v}\sin^2(2\pi f_d t), & t_1 \le t \le t_1 + t_d \\ 0, & \text{otherwise} \end{cases} \tag{13}$$

where $f_d = 200$ Hz and $t_d = 2.5$ ms resulting in a non-zero frequency content within -750 to 850 Hz. The impulse can be seen as a continuous distribution of excitation frequencies which all have the same phase angle.

The influence of the direction is studied by varying φ between 0 and 2π rad. As an example, Fig. 3*a* presents the FRF obtained at $\varphi = 0$ and Fig. 3*b* at $\varphi = \pi/2$ with $a_{rel} = 0.1\%$. The comparison between the FRF obtained with harmonic excitation and the average of the two FRFs presented in Fig. 3 is shown in Fig. 4. The FRFs are shown in the stator reference frame.

Fig. 3 shows that the FRFs obtained using the unidirectional impulses contain a high additional peak ~100 Hz when compared with the FRF obtained from the

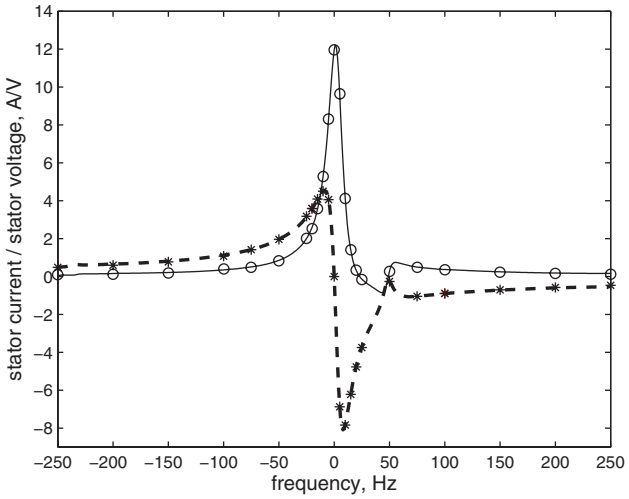

Fig. 4 *Comparison between the FRF obtained with harmonic excitation (o, real part; *, imaginary part) and the average of FRFs computed with $\varphi = 0$ and $\varphi = \pi/2$ (real part with solid line, imaginary part with dashed line)*

harmonic excitation in Fig. 4. Excess peaks also occur at -200, ± 300, 400, -500 and ± 600 Hz, but for the purpose of estimating the parameters of model (9), the frequency range can be limited to -200 to 200 Hz or less. Fig. 4 shows that taking the average of the FRFs presented in Fig. 3 removes the excess frequency components $\sim$100 Hz. When considering a wider frequency range, it can be noticed that the excess peaks at -200, 400 and -500 Hz are cancelled as well. The resulting average FRF in Fig. 4 is very close to the one obtained with the harmonic excitation. Only at 50 Hz, the difference between the imaginary parts is 20% and otherwise $<2\%$.

When considering the FRFs obtained using different direction angles between 0 and 2π, the similar effect as presented in Figs. 3 and 4 can be observed. Taking the average of any of the two FRFs from the perpendicular impulses cancels the excess frequency components. The phenomena can be studied more closely using the harmonic excitation with different phase angles. In that case, the excess peaks and their behaviour in relation with the phase angle can be distinguished from the desired frequency components. The reasons behind the additional frequency components and their cancellation are discussed in Sections 4 and 6. It is concluded that the excess frequency components related to the saturation of teeth can be cancelled or reduced based on the influence of the phase shift.

2.4 Curve-fitting technique

The parameters are estimated minimising the error between the simulated FRF and the FRF given by model (9). The curve fitting is performed in the stator reference frame and therefore ω_k is set to zero in (9). The cost function I is defined as

$$I = \sum_{n=1}^{N} \left(\mathrm{Re}\{y_m^n\} - \mathrm{Re}\{y_e^n\}\right)^2 + \left(\mathrm{Im}\{y_m^n\} - \mathrm{Im}\{y_e^n\}\right)^2 \tag{14}$$

n is the index and N the length of the data vector. Subscript m refers to the FRF obtained from the impulse method and subscript e refers to the FRF from model (9) with parameter estimates. The parameters are estimated first using a global optimisation technique differential evolution (DE) [15] and then refined with gradient-based Levenberg–Marquardt algorithm. First, DE is used to find the neighbourhood of the minimum. The acceptable values of the parameters are limited to the range of 0–10. The crossover probability CR and weighting factor F are set to 1.0. Typically, within <1000 function evaluations, the neighbourhood of the minimum is found. The obtained parameter estimates are given as initial values for the L–M algorithm. This way the number of iterations needed with DE can be reduced.

3 Results

A 37-kW cage-induction motor with closed rotor slots is studied. The rated values are given in Table 1 and the shape of the rotor and stator slots are shown in Fig. 5.

Both the estimation methods are based on the two-dimensional FEA where the effects of the end-rings and stator-end windings are taken into account by the end resistances and reactances. The details of the methods are given in [1]. The finite-element mesh consists of 1516 second-order triangular elements. In the simulations, the temperature of the stator windings is 98 °C and rotor cage 135 °C. The stator resistance given to the FE model is 0.083573 Ω.

3.1 Steady-state parameters

The estimated steady-state parameters of the single-cage and double-cage circuit models are presented in Table 2. For the comparison, the parameters for the linearised FE model with a relative permeability $\mu_r = 1000$ are also estimated. The rotor resistances are to be divided by the slip when substituted into the circuit model.

The total rotor resistance of the double-cage model is 0.06681 Ω and reactance is 0.4829 Ω. These are close to the corresponding values of the single-cage model. It can be noticed that the first rotor branch is practically resistive. If $X_{\sigma r1}$ is neglected, the total rotor reactance is decreased with only 0.07%. With the linear material, estimated $X_{\sigma r1}$ is negative. This is associated with the reference of the rotor variables to the stator. For the two cages, separate reference factors are computed in order to obtain a more accurate estimate for the electromagnetic torque [14]. On the other hand, the magnetic coupling between the two cages in the same rotor slots has a very small leakage. After the reference to the stator, the self-reactance can become slightly smaller than the mutual reactance. This phenomenon occurs at high loads.

Table 1: Parameters for the 37-kW cage-induction motor

P_N, kW	rated power	37
U_{sN}, V	rated stator voltage	380 (star)
p	number of pole pairs	2
f_N, Hz	rated stator frequency	50
s_N, %	rated slip	2
d_r, mm	diameter of the rotor	198
h_{rs}, [mm]	height of the rotor slot	35
J, kg m^2	inertia of the rotor	0.256

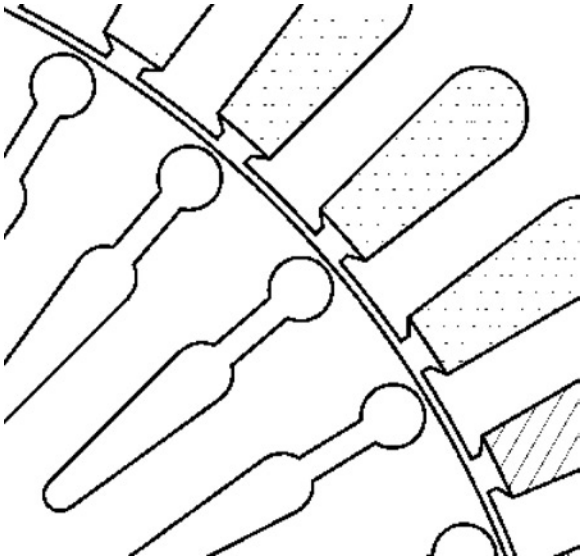

Fig. 5 *Cross-sectional geometry of the rotor and stator slots*

3.2 Small-signal parameters

The transfer function (9) contains nine parameters from which the stator resistance is known the basis of the FE model. As in the case of the single-cage model, the ratio between the stator and rotor leakage reactance has to be set. In addition, in the double-cage model, there are two equal rotor voltage equations. With a nonlinear curve fitting procedure, a good fit can be found by allowing all the parameters to vary. However, there are several sets of parameters which can give an equal fit. The parameter estimation for the induction machine has been analysed in [13]. The double-cage model with eight circuit parameters (r_c neglected) has only six independent parameters. Therefore the first aim is to reduce the number of the estimates. On the basis of inspection of the steady-state parameters, leakage inductance $l_{\sigma r1}$ is neglected. The ratio of the stator and rotor leakage reactance has to be fixed. The value of leakage inductance $l_{\sigma r1}$ is not estimated but solved from the estimated values of r_1, r_2, $l_{\sigma s}$ and l_c. The ratio of the total rotor leakage reactance and stator leakage reactance is set to the ratio of the corresponding steady-state parameters.

In addition to these constraints, the value of the mutual resistance is set beforehand. The simplest alternative is to neglect r_c and assume that it is included in the two other rotor resistances. However, the physical interpretation of the model is now changed because the resistive coupling between the rotor branches is lost. Hence, it is assumed that the mutual resistance is obtained from the estimation of steady-state parameters and the same value can be used for the small-signal model.

Three different cases are studied:

1. The impulse response test is performed for the linearised FE model with $\mu_r = 1000$. Since the saturation is eliminated, the shape of the impulse is not crucial.
2. The impulse test is performed with the impulse defined by (11) for the nonlinear FE model where the permeability is defined by the magnetisation curve. This is referred as nonlinear case A.
3. The impulse test is performed with impulses defined by (13) and aligned with a certain angle to the total voltage vector. The FRF is calculated using the average of the two impulse tests obtained with perpendicular impulses with $\varphi = 0$ and $\varphi = \pi/2$. The cases $\varphi = \pi/6$ and $\varphi = 2\pi/3$, $\varphi = \pi/4$ and $\varphi = 3\pi/4$, and $\varphi = \pi/3$ and $\varphi = 5\pi/6$ are also studied. The effect of the amplitude is studied by varying a_{rel} between 0.1 and 50%. Using the average of two FRFs is referred as nonlinear case B.

The fit is performed for the frequency range of -200 to 200 Hz with the resolution of 1 Hz. The estimated small-signal parameters are presented in Table 3. The fixed parameters are marked by asterisk and the calculated rotor leakage reactance $x_{\sigma r2}$ is marked by two asterisks.

The value of the cost function (15) presented in the last row of Table 3 gives an idea about the goodness of the fit. For the linearised machine, the difference between the simulated and estimated FRFs is $<1\%$ in the whole range studied. For nonlinear case A, the fit is otherwise fairly good but in the range of 40–200 Hz the difference is 15–20% which causes the high value for the cost function. For nonlinear case B, the difference is 0.1–3%, except at ± 200 Hz where it is $\sim 5\%$.

When the frequency response data are fitted to transfer function (9), the requirement of the physically meaningful parameters may limit the goodness of the fit. A traditional method to fit the frequency response data was presented by Levi [16]. The algorithm is available in Matlab®. In the method, the orders of the numerator and denominator are chosen in advance. The estimated coefficients are those which provide the best fit. For nonlinear case B, the

Table 2: Steady-state parameters for the linear and nonlinear FE models

	1-cage (linear)	2-cage (linear)	1-cage (nonlinear)	2-cage (nonlinear)
R_s, Ω	0.08357	0.08357	0.08357	0.08357
$X_{\sigma s}$, Ω	0.2460	0.2459	0.2476	0.2464
X_m, Ω	7.640	7.640	8.431	8.432
X_c, Ω	—	0.17732	—	0.3348
R_c, Ω	—	0.01539	—	0.01539
$X_{\sigma r1}$, Ω	0.30609	−0.02262	0.4815	0.00473
R_{r1}, Ω	0.06775	0.2060	0.06681	0.1975
$X_{\sigma r2}$ Ω	—	0.2341	—	0.2700
$R_{\sigma r1}$, Ω	—	0.07013	—	0.06942

Table 3: Estimated small-signal parameters

	Linear	Nonlinear A	Nonlinear B
r_s, Ω	0.08357*	0.08357*	0.08357*
$X_{\sigma s}$, Ω	0.1818	0.1772	0.1945
x_m, Ω	6.910	3.785	4.310
x_c, Ω	0.2041	0.1959	0.1937
r_c, Ω	0.01539*	0.01539*	0.01539*
$x_{\sigma r1}$, Ω	0*	0*	0*
r_{r1}, Ω	0.2395	0.1921	0.2784
$x_{\sigma r2}$, Ω	0.2545**	0.27310**	0.2979**
r_{r2}, Ω	0.07029	0.06604	0.07245
l	0.2118	3.820	0.3859

transfer function obtained is

$$\frac{\Delta i_s(s)}{\Delta \underline{u}_s(s)} = \frac{\begin{array}{l}(845.1 - \mathrm{j}12.68)s^2 \\ +(3.11 \cdot 10^5 - \mathrm{j}5.691 \cdot 10^5)s \\ -9.378 \cdot 10^7 - \mathrm{j}9.73 \cdot 10^7\end{array}}{\begin{array}{l}s^3 + (681.3 - \mathrm{j}705.0)s^2 \\ +(7.444 \cdot 10^4 + \mathrm{j}2.401 \cdot 10^5)s \\ -7.83 \cdot 10^6 - \mathrm{j}8.108 \cdot 10^6\end{array}} \quad (15)$$

For the comparison, the transfer function obtained by substituting the estimated small-signal parameters from Table 3 into (9) is

$$\frac{\Delta i_s(s)}{\Delta \underline{u}_s(s)} = \frac{\begin{array}{l}826.8s^2 + (3.228 \cdot 10^5 + \mathrm{j}1.039 \cdot 10^4)s \\ +1.522 \cdot 10^6 + \mathrm{j}2.028 \cdot 10^6\end{array}}{\begin{array}{l}s^3 + (682.0 + \mathrm{j}326.7)s^2 \\ +(4.529 \cdot 10^4 + \mathrm{j}1.973 \cdot 10^5)s \\ -1.083 \cdot 10^6 + \mathrm{j}7.162 \cdot 10^6\end{array}} \quad (16)$$

The coefficients of the higher-order terms are of the same magnitude. The most significant difference is in the signs of the coefficients. In (16), the parameters can have only positive values and the signs of the coefficients are determined by the assumption. In (15), both the signs and the magnitudes of the coefficients can vary during the estimation. This gives more freedom for finding the best model. The cost function for (15) is 0.1692 which is less than half of the corresponding value for (16). However, both the models are feasible when considering the goodness of the fit.

3.3 Small-signal model

The parameter estimation is performed assuming a uniform air-gap length so that the complex-valued voltages and currents can be used. In this case, the coefficients of the transfer function are complex as well. However, in order to study the small-signal behaviour, the state-space model is usually presented. To obtain the state-space model, the voltage and flux equations (1)–(6) are divided into real and imaginary parts and resulting 12 equations are linearised. The linearised equation of motion is also added in order to include perturbations of load torque in the model. The linearised equation of electromagnetic torque contains steady-state current components. The steady-state stator current can be obtained from time-stepping analysis at the initial state preceding the impulse test (Table 4). The components of rotor current are obtained by the current division using the circuit model (Fig. 1) and the steady-state parameters from Table 2.

The completed small-signal model is presented in Section 6. In [5], the axes of the small-signal model were aligned with and perpendicular to the air-gap voltage and the two different values for the magnetising inductance were applied. Here, the estimated parameters are those providing the best fit and they are substituted into the state-space model assuming the symmetry of the axes. One application of the small-signal model is evaluating the stability of the system about the operation point. The stability limits can be defined from the eigenvalues of the state-space model. The basic requirement for the stability is that the real parts of the eigenvalues are negative. The further from the origin they are, the more stable the system is. In order to evaluate the effect of different parameter estimates, the eigenvalues are calculated using both the steady-state parameters and the small-signal parameters given by nonlinear case B. The eigenvalues are presented in Table 5.

The real parts of the eigenvalues given by the small-signal parameters are further from the origin than those given by the steady-state parameters. Using the steady-state parameters in the study of small-signal behaviour, the stability limits obtained are too pessimistic. The similar effect has been detected in [5].

Table 4: Steady-state currents

i^0_{sa}, A	83.00
i^0_{sb}, A	−56.32
i^0_{r1a}, A	−22.79
i^0_{r1b}, A	4.16
i^0_{r2a}, A	−63.55
i^0_{r2b}, A	16.76

Table 5: Eigenvalues calculated using the steady-state and the small-signal parameters

Steady-state		Nonlinear B	
Re	Im	Re	Im
−417.74	±12.106	−626.21	±16.605
−45.176	±303.59	−50.625	±298.54
−16.095	±97.458	−21.141	±51.337
−26.288	0	−32.943	0

4 Discussion

4.1 Frequency components related to saturation

On the basis of the study, it can be concluded that the saturation caused by the fundamental air-gap flux makes the magnetic circuit of the machine anisotropic. When the magnetic field induced by the perturbation signal faces the anisotropic magnetic circuit, the additional frequency components in the air-gap flux and stator current are produced. Next, the features of the excess harmonics are discussed in more detail.

As presented in Section 6, the additional peak occurring in the FRF around twice the supply frequency (100 Hz) is related to the permeance variation caused by the saturation of teeth. According to the theory, at every excitation frequency f_d, the current response should contain a peak at $100 - f_d$ Hz. The assumption can be tested within the time-stepping analysis. The shape of the rotor of the FE model is modified to have a slightly square shape. The length of the air gap is widest in the region of the highest flux density. When the material of the FE model is set linear, the effects of the real saturation are removed and the model imitates the situation when only the teeth are saturated. If the rotor is rotating at the synchronous speed, the excess harmonics caused by the permeance variations should occur at the same frequencies as detected with the real, saturable FE model. The assumption is tested by performing the harmonic excitation at several excitation frequencies. The computation results show that the additional frequency peak do occur at $100 - f_d$ Hz, for example, with 120 Hz excitation at −20 Hz and with −14 Hz excitation at 114 Hz. As the amplitude of the response is highest at low frequencies, the effect of excess harmonics is mostly visible ∼100 Hz.

With the harmonic excitation, the effect of the phase angle can be studied more closely. When the voltage excitation is shifted by phase angle φ with respect to the supply voltage, the current response at the corresponding frequency is also shifted by φ. However, the amplitudes of the vectors remain the same. When they are divided, the effect of the phase shift vanishes. Thus the resulting FRF does not depend on the phase angle of excitation. Only with the 50 Hz excitation, the magnitude of the imaginary part varies within 16% when the phase angle is changed. In this case, the excitation signal has the same frequency with the supply voltage and cancelling the steady state may be inaccurate. This can also explain the deviation between the results of the impulse test and harmonic excitation at 50 Hz.

The FRF obtained by the impulse excitation can be seen to consist of two parts. At each frequency, the current response contains a component excited by the corresponding frequency component of the excitation signal. In addition to that the current response contains the components excited by other frequencies. When the voltage excitation is shifted by phase angle φ, the phase of the detected excess harmonic at $100 - f_d$ Hz is shifted by $-\varphi$, as shown in Section 6.1. When the excess harmonic component is divided by the excitation signal, where all the frequency components are shifted by φ, the phase shift for the harmonic component in the FRF is 2φ. Similarly, if the excitation signal is shifted by $\varphi + \pi/2$, the excess harmonic component in the FRF is shifted by $2\varphi + \pi$. Calculating the average of these FRFs cancels the harmonic components at frequency $100 - f_d$.

The excess frequency peaks at $100 - f_d$ Hz are so significant that, if not reduced, they distort the parameter estimation. In [17], the numerical impulse test was performed for an 850-kW cage-induction machine with half-open rotor slots. In that case, the effect of the excess harmonics was small and could be omitted. In the case of the closed rotor slots, the saturation has a more important influence. In [18], the effect of the slot closure has been studied by means of the FEA. The authors have concluded that when the rotor slots are closed, the harmonics related to saturation are magnified significantly.

4.2 Effect of the amplitude

The effect of the amplitude of the impulse is studied by varying a_{rel} between 0.1 and 50%. The impulse tests are performed with both positive and negative values for a_{rel}. For every a_{rel}, the impulse tests are performed with the direction angles 0 and $\pi/2$. The parameter estimation is performed using the average of the two FRFs as presented in Section 2.

With $a_{rel} = 0.1-15\%$, the FRFs change very little which is best detected from the parameter estimates. Rotor resistance r_{r1} decreases by 4.9% and the magnetising inductance increases by 3.4%, but with the other parameters the differences are very small. The fit is improved when increasing the amplitude and is at its best with $a_{rel} = 15-20\%$. With very low excitation amplitudes, the accuracy of the computation results may weaken. With the relative amplitudes $>20\%$, the fit begins to deteriorate again. However, the parameter estimates obtained remain close to the same magnitude. For example, at $a_{rel} = 50\%$, the value of the magnetising inductance is 9.0% higher than the value obtained at $a_{rel} = 0.1\%$. The minor influence of the amplitude speaks for the conclusion that the effects of nonlinearity are mainly related to saturation caused by the fundamental flux.

The presented paper is lacking measurements. In [4], the steady-state parameters of the T-equivalent circuit for the studied motor were measured. In comparison with the measurements, the estimated parameters were concluded to be physically reasonable. However, the impulse test and the harmonic excitation are to be performed by measurements. The main challenge is distinguishing the steady-state frequencies from the impulse response. The measurement setup is currently under development.

As a summary, three computations are needed to perform a comprehensive impulse test. The impulse is applied in two perpendicular directions. A steady-state computation is needed to cancel the supply frequency from the frequency response. The effect of the harmonics can be reduced by taking the average of the two FRFs obtained using perpendicular impulses.

5 Conclusions

The applicability of the numerical impulse response test for estimating the small-signal parameters has been studied. The main focus was on taking into account the skin effect in the deep-bar rotor with closed slots. The rotor was modelled with two parallel branches consisting of five constant parameters. Since the use of the impulse test is based on the assumption of linear behaviour about an operation point, the effects of nonlinearity were also studied. In addition to the full FE model, the computations were performed using a modified FE model with linearised material and non-uniform air gap. In the computations, both the amplitude and phase angle of the excitation signal were varied. On the basis of the computations and theoretical study, it can be concluded that the anisotropy of the magnetic circuit produces additional frequency components to the frequency response of the stator current. However, the excess harmonics can be distinguished from the desired frequency components. The obtained parameter estimates are physically reasonable and the values of inductances are related to the incremental permeability as expected.

6 References

1 Arkkio, A.: 'Analysis of induction motors based on the numerical solution of the magnetic field and circuit equations', Electrical Engineering Series, No. 59, Acta Polytechnica Scandinavica, Helsinki, 1987, p. 97 Available http://lib.tkk.fi/Diss/198X/isbn951226076X/

2 Williamson, S., and Begg, M.C.: 'Analysis of cage induction motors – a combined fields and circuits approach', *IEEE Trans. Mag.*, 1985, **Mag-21**, (6), pp. 2396–2399

3 Williamson, S., and Gersh, D.R.: 'Finite element calculation of double-cage equivalent circuit parameters', *IEEE Trans. Energy Convers.*, 1996, **11**, (1), pp. 41–48

4 Repo, A.-K., and Arkkio, A.: 'Numerical impulse response test to estimate circuit-model parameters for induction machines', *IEE Proc. Electr. Power Appl.*, 2006, **153**, (6), pp. 883–890

5 Melkebeek, J.A.A., and Novotny, D.W.: 'The Influence of Saturation on Induction Machine Drive Dynamics', *IEEE Trans. Ind. Appl.*, 1983, **IA-19**, (5), pp. 671–681

6 Smith, A.C., Healey, R.C., and Williamson, S.: 'A transient induction motor model including saturation and deep bar effect', *IEEE Trans. Energy Convers.*, 1996, **11**, (1), pp. 8–15

7 Levi, E.: 'Main flux saturation modelling in double-cage and deep-bar induction machines', *IEEE Trans. Energy Convers.*, 1996, **11**, (2), pp. 305–311

8 Thiringer, T.: 'Measurements and modelling of low-frequency disturbances in induction machines'. Doctoral thesis, Chalmers University of Technology, 1996, p. 130

9 Sudhoff, S.D., Aliprantis, D.C., Kuhn, B.T., and Chapman, P.L.: 'An induction machine model for predicting inverter-machine interaction', *IEEE Trans. Energy Convers*, 2002, **17**, (2), pp. 203–210

10 Luomi, J., Niemenmaa, A., and Arkkio, A.: 'On the use of effective reluctivities in magnetic field analysis of induction motors fed from a sinusoidal voltage source'. Proc. Int. Conf. Electrical Machines, Munich, Germany, 1986 (Technische Universität München), vol. 2, pp. 706–709

11 Krause, P.C., Wasynczuk, O., and Sudhoff, S.D.: 'Analysis of electric machinery and drive systems' (John Wiley & Sons, 2002, 2nd edn.)
12 Corcoles, F., Pedra, J., Salichs, M., and Sainz, L.: 'Analysis of induction machine parameter identification', *IEEE Trans. Energy Convers.*, 2002, **17**, (2), pp. 183–190
13 Retiere, N., Foggia, A., Roye, D., and Mannevy, P.: 'Deep-bar induction motor model for large transient analysis under saturated conditions'. IEEE Proc. Int. Conf. Electric Machines and Drives, Milwaukee, U.S., 1997, MD1/3.1–MD1/3.3
14 Repo, A.-K., Niemenmaa, A., and Arkkio, A.: 'Estimating circuit models for a deep-bar induction motor using time harmonic finite element analysis'. Proc. Int. Conf. Electrical Machines, Crete, Creece, 2006, [IEEE], on CD No. 614
15 Price, K.V., Storn, R.M., and Lampinen, J.A.: 'Differential evolution: a practical approach to global optimization' (Springer Berlin, 2005)
16 Levi, E.C.: 'Complex-curve fitting', *IRE Trans. Autom. Control*, 1959, **AC-4**, pp. 37–44
17 Repo, A.-K., and Arkkio, A.: 'Parameter estimation of induction machines using the numerical impulse method'. Proc. SPEEDAM, Taormina, Italy, 2006, [IEEE], on CD No. WA1-19136
18 Salon, S., Burow, D., DeBortoli, M., and Slavik, C.: 'Effects of slot closure and magnetic saturation on induction machine behaviour', *IEE Trans. Mag*, 1994, **30**, (30), pp. 3697–3700
19 Jokinen, T.: 'Utilization of harmonics for self-excitation of a synchronous generator by placing an auxiliary winding in the rotor', Electrical Engineering Series, No. 32 thesis, Acta Polytechnica Scandinavica, Helsinki, 1973, p. 82 Available http://lib.tkk.fi/Diss/197X/isbn9512260778/

7 Appendices

7.1 Appendix A

Saturation of iron in the teeth or yoke changes the permeance. The effect of saturation can be modelled by a non-uniform air gap which can be represented as Fourier series [19]. The teeth are mostly saturated along the peak value of flux density, where the apparent air gap is the widest. The permeance of the air gap can be considered as

$$\Lambda \simeq \frac{\mu_0}{\delta_0 + \sum_\upsilon \delta_\upsilon \cos(\upsilon\theta - \upsilon\omega_s t - \varphi_\upsilon)} \tag{17}$$

where $\upsilon = k \cdot 2p$, $k = 1, 2, 3, \ldots$. Permeance wave υ produces the apparent air-gap component δ_υ. ω_s is the supply frequency (50 Hz), φ_υ is the phase angle and θ the position angle. Next, only the permeance waves $\upsilon = 2$ and $\upsilon = 4$ are considered. The ratio δ_4/δ_2 is denoted with w. When the equation is expanded to Taylor series with respect to the air gap and only the first three terms are considered, the air gap permeance can be approximated

$$\begin{aligned}\Lambda \simeq \frac{\mu_0}{\delta_0}\Bigg[& 1 - \frac{\delta_{\upsilon 2}}{\delta_0}\cos(2p\theta - 2\omega_s t - \varphi_{\upsilon 2}) \\ & - \frac{w\delta_{\upsilon 2}}{\delta_0}\cos(4p\theta - 4\omega_s t - \varphi_{\upsilon 4}) \\ & + \frac{1}{2}\left(\frac{\delta_{\upsilon 2}}{\delta_0}\right)^2 (1 + \cos(4p\theta - 4\omega_s t - 2\varphi_{\upsilon 2})) \\ & + w\left(\frac{\delta_{\upsilon 2}}{\delta_0}\right)^2 [\cos(6p\theta - 6\omega_s t - (\varphi_{\upsilon 2} + \varphi_{\upsilon 4})) \\ & + \cos(-2p\theta + 2\omega_s t - (\varphi_{\upsilon 2} - \varphi_{\upsilon 4}))] \\ & + \frac{1}{2}\left(\frac{w\delta_{\upsilon 2}}{\delta_0}\right)^2 (1 + \cos(8p\theta - 8\omega_s t - 2\varphi_{\upsilon 4}))\Bigg]\end{aligned} \tag{18}$$

The magnetomotive force (mmf) related to the disturbance frequency is

$$F = \hat{F}\cos(p\theta - \omega_d t - \varphi_d) \tag{19}$$

The amplitudes of the space harmonics of the mmf are small and their effect is neglected. When multiplying the cosine terms, the final equation for the air-gap flux density is obtained

$$\begin{aligned}B = \hat{F}\frac{\mu_0}{\delta_0}\Bigg[& \left(1 + \frac{1}{2}\left(\frac{\delta_{\upsilon 2}}{\delta_0}\right)^2 + \frac{1}{2}\left(\frac{w\delta_{\upsilon 2}}{\delta_0}\right)^2\right) \\ & \times \cos(p\theta - \omega_d t - \varphi_d) \quad (1\,\text{terms}) \\ & - \frac{\delta_{\upsilon 2}}{2\delta_0}\begin{pmatrix}\cos(3p\theta - (2\omega_s + \omega_d)t \\ -(\varphi_{\upsilon 2} + \varphi_d)) + \cos(p\theta \\ -(2\omega_s - \omega_d)t - (\varphi_{\upsilon 2} - \varphi_d))\end{pmatrix} \quad (2,3\,\text{terms}) \\ & - \frac{w\delta_{\upsilon 2}}{2\delta_0}\begin{pmatrix}\cos(5p\theta - (4\omega_s + \omega_d)t \\ -(\varphi_{\upsilon 4} + \varphi_d)) + \cos(3p\theta \\ -(4\omega_s - \omega_d)t - (\varphi_{\upsilon 4} - \varphi_d))\end{pmatrix} \quad (4,5\,\text{terms}) \\ & + \frac{1}{4}\left(\frac{w\delta_{\upsilon 2}}{\delta_0}\right)^2\begin{pmatrix}\cos(5p\theta - (4\omega_s + \omega_d)t \\ -(2\varphi_{\upsilon 2} - \varphi_d)) + \cos(3p\theta \\ -(4\omega_s - \omega_d)t - (2\varphi_{\upsilon 2} - \varphi_d))\end{pmatrix} \quad (6,7\,\text{terms}) \\ & + \frac{w}{2}\left(\frac{\delta_{\upsilon 2}}{\delta_0}\right)^2\begin{pmatrix}\cos(7p\theta - (6\omega_s + \omega_d)t \\ -(\varphi_{\upsilon 2} + \varphi_{\upsilon 2} + \varphi_d)) \\ +\cos(5p\theta - (6\omega_s - \omega_d)t \\ -(\varphi_{\upsilon 2} + \varphi_{\upsilon 2} - \varphi_d))\end{pmatrix} \quad (8,9\,\text{terms}) \\ & + \frac{w}{2}\left(\frac{\delta_{\upsilon 2}}{\delta_0}\right)^2\begin{pmatrix}\cos(-p\theta - (2\omega_s + \omega_d)t \\ -(\varphi_{\upsilon 2} + \varphi_{\upsilon 2} + \varphi_d)) \\ +\cos(-3p\theta - (-2\omega_s - \omega_d)t \\ -(\varphi_{\upsilon 2} + \varphi_{\upsilon 2} - \varphi_d))\end{pmatrix} \\ & \qquad (10,11\,\text{terms}) \\ & + \frac{1}{4}\left(\frac{w\delta_{\upsilon 2}}{\delta_0}\right)^2\begin{pmatrix}\cos(9p\theta - (8\omega_s + \omega_d)t \\ -(2\varphi_{\upsilon 4} + \varphi_d)) + \cos(7p\theta \\ -(8\omega_s - \omega_d)t \\ -(2\varphi_{\upsilon 4} - \varphi_d))\end{pmatrix} \quad (12,13\,\text{terms})\Bigg]\end{aligned} \tag{20}$$

The flux density consists of a component rotating at the fundamental frequency and 12 other components, whose amplitudes depend on the permeance wave. Since the frequency range used for the parameter estimation is −200 to 200 Hz, the effect of higher-order permeance waves can be neglected. All the components of the flux density are not present in the line current. The stator of the studied motor is star connected. Therefore the components having wave numbers $\pm 3p$ and $9p$ cannot induce currents in the winding. The winding factor for the fifth harmonic is only 0.2 and therefore the fourth, sixth and ninth terms are small. In general, the small coefficients in front of the last eight terms reduce their amplitude. Thus, the most significant frequency component caused by the saturation of teeth is the third term at $100 - f_d$ Hz. It should be noticed that the sign of the phase angle φ_d is minus in the fundamental component but plus in the third term.

7.2 Appendix B

The small-signal model for the double-cage circuit is derived from (1) to (7).

$$\begin{bmatrix} \Delta u_{sx} \\ \Delta u_{sy} \\ 0 \\ 0 \\ 0 \\ 0 \\ \Delta T_L \end{bmatrix} = \begin{bmatrix} r_s+Dl_s & -\omega_k^0 l_s & Dl_m & -\omega_k^0 l_m \\ \omega_k^0 l_s & r_s+Dl_s & \omega_k^0 l_m & Dl_m \\ Dl_m & (\omega_r^0-\omega_k^0)l_m & r_c+r_{r1}+Dl_{r1}^* & (\omega_r^0-\omega_k^0)l_{r1}^* \\ -(\omega_r^0-\omega_k^0)l_m & Dl_m & -(\omega_r^0-\omega_k^0)l_{r1}^* & r_c+r_{r1}+Dl_{r1}^* \\ Dl_m & (\omega_r^0-\omega_k^0)l_m & Dl_c^*+r_c & (\omega_r^0-\omega_k^0)l_c^* \\ -(\omega_r^0-\omega_k^0)l_m & Dl_m & -(\omega_r^0-\omega_k^0)l_c^* & Dl_c^*+r_c \\ -\frac{3}{2}pl_m(i_{r1y}^0+i_{r2y}^0) & \frac{3}{2}pl_m(i_{r1x}^0+i_{r2x}^0) & \frac{3}{2}pl_m i_{sy}^0 & -\frac{3}{2}pl_m i_{sx}^0 \end{bmatrix}$$

$$\begin{bmatrix} Dl_m & -\omega_k^0 l_m & 0 \\ \omega_k^0 l_m & Dl_m & 0 \\ Dl_c^*+r_c & (\omega_r^0-\omega_k^0)l_c^* & l_m i_{sy}^0+l_{r1}^* i_{r1y}^0+l_c^* i_{r2y}^0 \\ -(\omega_r^0-\omega_k^0)l_c^* & Dl_c^*+r_c & -l_m i_{sx}^0-l_{r1}^* i_{r1x}^0-l_c^* i_{r2x}^0 \\ r_c+r_{r2}+Dl_{r2}^* & (\omega_r^0-\omega_k^0)l_{r2}^* & l_m i_{sy}^0+l_{r2}^* i_{r2y}^0+l_c^* i_{r1y}^0 \\ -(\omega_r^0-\omega_k^0)l_{r2}^* & r_c+r_{r2}+Dl_{r2}^* & -l_m i_{sx}^0-l_{r2}^* i_{r2x}^0-l_c^* i_{r1x}^0 \\ \frac{3}{2}pl_m i_{sy}^0 & -\frac{3}{2}pl_m i_{sx}^0 & -D\frac{J}{p} \end{bmatrix}$$

$$\begin{bmatrix} \Delta i_{sx} \\ \Delta i_{sy} \\ \Delta i_{r1x} \\ \Delta i_{r1y} \\ \Delta i_{r2x} \\ \Delta i_{r2y} \\ \Delta \omega_r \end{bmatrix} \tag{21}$$

D is the time-derivative operator. The short-notations are

$$\begin{aligned} l_s &= l_m + l_{\sigma s} \\ l_c^* &= l_m + l_c \\ l_{r1}^* &= l_m + l_c + l_{\sigma r1} \\ l_{r2}^* &= l_m + l_c + l_{\sigma r2} \end{aligned} \tag{22}$$

When separating the derivatives, (B1) can be written as

$$\boldsymbol{E}D\boldsymbol{x} = \boldsymbol{F}\boldsymbol{x} + \boldsymbol{u} \tag{23}$$

where

$$\mathbf{x}^T = \begin{bmatrix} \Delta i_{sx} & \Delta i_{sy} & \Delta i_{r1x} & \Delta i_{r1y} & \Delta i_{r2x} & \Delta i_{r2y} & \Delta \omega_r \end{bmatrix} \tag{24}$$

$$\mathbf{u}^T = \begin{bmatrix} \Delta u_{sx} & \Delta u_{sy} & \Delta u_{r1x} & \Delta u_{r1y} & \Delta u_{r2x} & \Delta u_{r2y} & \Delta T_L \end{bmatrix} \tag{25}$$

$$\mathbf{E} = \begin{bmatrix} l_s & 0 & l_m & 0 & l_m & 0 & 0 \\ 0 & l_s & 0 & l_m & 0 & l_m & 0 \\ l_m & 0 & l_{r1}^* & 0 & l_c^* & 0 & 0 \\ 0 & l_m & 0 & l_{r1}^* & 0 & l_c^* & 0 \\ l_m & 0 & l_c^* & 0 & l_{r2}^* & 0 & 0 \\ 0 & l_m & 0 & l_c^* & 0 & l_{r2}^* & 0 \\ 0 & 0 & 0 & 0 & 0 & 0 & -\frac{J}{p} \end{bmatrix} \tag{26}$$

$$F = -\begin{bmatrix} r_s & -\omega_k^0 l_s & 0 \\ \omega_k^0 l_s & r_s & \omega_k^0 l_m \\ 0 & (\omega_r^0-\omega_k^0)l_m & r_c+r_{r1} \\ -(\omega_r^0-\omega_k^0)l_m & 0 & -(\omega_r^0-\omega_k^0)l_{r1}^* \\ 0 & (\omega_r^0-\omega_k^0)l_m & r_c \\ -(\omega_r^0-\omega_k^0)l_m & 0 & -(\omega_r^0-\omega_k^0)l_c^* \\ -\frac{3}{2}pl_m(i_{r1y}^0+i_{r2y}^0) & \frac{3}{2}pl_m(i_{r1x}^0+i_{r2x}^0) & \frac{3}{2}pl_m i_{sy}^0 \end{bmatrix}$$

$$\begin{bmatrix} -\omega_k^0 l_m & 0 \\ 0 & \omega_k^0 l_m \\ (\omega_r^0-\omega_k^0)l_{r1}^* & r_c \\ r_c+r_{r1} & -(\omega_r^0-\omega_k^0)l_c^* \\ (\omega_r^0-\omega_k^0)l_c^* & r_c+r_{r2} \\ r_c & -(\omega_r^0-\omega_k^0)l_{r2}^* \\ -\frac{3}{2}pl_m i_{sx}^0 & \frac{3}{2}pl_m i_{sy}^0 \end{bmatrix}$$

$$\begin{bmatrix} -\omega_k^0 l_m & 0 \\ 0 & 0 \\ (\omega_r^0-\omega_k^0)l_c^* & l_m i_{sy}^0+l_{r1}^* i_{r1y}^0+l_c^* i_{r2y}^0 \\ r_c & -l_m i_{sx}^0-l_{r1}^* i_{r1x}^0-l_c^* i_{r2x}^0 \\ (\omega_r^0-\omega_k^0)l_{r2}^* & l_m i_{sy}^0+l_{r2}^* i_{r2y}^0+l_c^* i_{r1y}^0 \\ r_c+r_{r2} & -l_m i_{sx}^0-l_{r2}^* i_{r2x}^0-l_c^* i_{r1x}^0 \\ -\frac{3}{2}pl_m i_{sx}^0 & 0 \end{bmatrix} \tag{27}$$

The state-space model is defined by

$$\begin{aligned} D\boldsymbol{x} &= \boldsymbol{A}\boldsymbol{x} + \boldsymbol{B}\boldsymbol{u} \\ \boldsymbol{A} &= \boldsymbol{E}^{-1}\boldsymbol{F} \\ \boldsymbol{B} &= \boldsymbol{E}^{-1} \end{aligned} \tag{28}$$

The eigenvalues of the system are the eigenvalues of matrix $\boldsymbol{A}$.